SANDIA REPORT

SAND2005-6555
Unlimited Release
Printed October 2005

On the Modeling, Design and Validation of Two Dimensional Quasi-static Eddy Currents Forces in a Mechanical Oscillator

John A. Mitchell
Surety Components and Instrumentation

Jonathan W. Wittwer
Microsystems, Science, Technology and Components

David S. Epp
Engineering Sciences

Prepared by
Sandia National Laboratories
Albuquerque, New Mexico 87185 and Livermore, California 94550

Sandia is a multiprogram laboratory operated by Sandia Corporation,
a Lockheed Martin Company, for the United States Department of Energy's
National Nuclear Security Administration under Contract DE-AC04-94-AL85000.

Sandia National Laboratories

Issued by Sandia National Laboratories, operated for the United States Department of Energy by Sandia Corporation.

Available to DOE and DOE contractors from
U.S. Department of Energy
Office of Scientific and Technical Information
P.O. Box 62
Oak Ridge, TN 37831

Telephone:	(865) 576-8401
Facsimile:	(865) 576-5728
E-Mail:	reports@adonis.osti.gov
Online ordering:	http://www.doe.gov/bridge

Available to the public from
U.S. Department of Commerce
National Technical Information Service
5285 Port Royal Rd
Springfield, VA 22161

Telephone:	(800) 553-6847
Facsimile:	(703) 605-6900
E-Mail:	orders@ntis.fedworld.gov
Online ordering:	http://www.ntis.gov/ordering.htm

SAND2005-6555
Unlimited Release
Printed October 2005

On the Modeling, Design and Validation of Two Dimensional Quasi-static Eddy Current Forces in a Mechanical Oscillator

John A. Mitchell and Jonathan W. Wittwer and David S. Epp
Sandia National Laboratories
1515 Eubank SE
Albuquerque, NM 87185

Abstract

Damping vibrations is important in the design of some types of inertial sensing devices. One method for adding damping to a device is to use magnetic forces generated by a static magnetic field interacting with eddy currents. In this report, we develop a 2-dimensional finite element model for the analysis of quasistatic eddy currents in a thin sheet of conducting material. The model was used for design and sensitivity analyses of a novel mechanical oscillator that consists of a shuttle mass (thin sheet of conducting material) and a set of folded spring elements. The oscillator is damped through the interaction of a static magnetic field and eddy currents in the shuttle mass. Using a prototype device and Laser Dopler Velocimetry (LDV), measurements were compared to the model in a validation study using simulation based uncertainty analyses. Measurements were found to follow the trends predicted by the model.

Acknowledgment

The authors would like to thank Rosemarie Renn and Rebecca Clemens for their work on the prototype mechanical oscillators including packaging, assembly and testing. We would also like to thank Nolan Finch for designing the mechanical oscillator and Jack Smith for creating the Pro-E drawings. The authors would also like to acknowledge the helpful discussions with Anton Sumali on test results.

Contents

1 Introduction 7
2 Mathematical Models 8
2.1 Eddy Currents 9
2.2 Magnetic Field 10
3 Finite Element Formulation 10
3.1 Magnetic Field 10
3.2 Eddy Currents 14
4 Modeling a Device 14
4.1 Magnetic Field 16
4.2 Eddy Currents 16
4.3 Calculating Damping Forces 18
4.4 Sensitivity Analysis 20
5 Correlation with Measurements 22
5.1 Experimental Setup and Measurement Results 22
5.2 Model Validation 27
6 Conclusions 29
References 31

Appendix

A Frequency Response Curve Fitting 33

Figures

1 Rectangle finite element shape functions 13
2 Damped Oscillator Schematic 15
3 Exploded View of Magnet Pairs (and magnetization) in Device 15
4 Magnetic field ($x-z$ plane): Shuttle conductor centered between 3 magnet pairs 17
5 Current $\vec{J}$ in $y-z$ plane: Magnets in blue overlay with $\vec{J}$ values plotted at the element centroids 18
6 Magnetic body force distribution 21
7 Damping ratio sensitivities: magnet spacing, gap, resistivity, magnetization, beam width 21
8 Picture of the test setup 22
9 Magnetic field in (x-z plane) enhanced by backplane: Shuttle conductor centered between 3 magnet pairs 24
10 Transmissibility measurements for eddy current demonstration without backing plate 25
11 Transmissibility measurements for eddy current demonstration with a backing plate 26

12 Uncertainty Analysis: 95 % Confidence Bands on damping ratio 29
13 Uncertainty contributions to damping ratio 30

Tables

1 Curve-fitting results for demonstration tests 23
2 Curve-fitting results for demonstration tests with a backing plate 25
3 Uncertainty analysis input data 27
4 Measured and calculated ζ: uncertainty analysis results (no back plate) . . . 28
5 Uncertainty Analysis Results (with backplane) 28

On the Modeling, Design and Validation of Two Dimensional Quasi-static Eddy Current Forces in a Mechanical Oscillator

1 Introduction

Magnetic forces generated by a static magnetic field interacting with eddy currents can be a novel means of damping vibrations. The existence and mechanisms for generation of eddy currents is well known and documented in the physics and engineering communities. Predictive modelling strategies are less well known although it is critically important for developing devices.

In this paper we focus on a simple mathematical model for quasi-static analyses that is particularly useful for modelling $2\frac{1}{2}$D applications in which a static magnetic field $\vec{B} = B_z\hat{k}$ is perpindicular to and pass through a thin sheet of conducting material. The thin sheet of material is non-magnetic and, for modelling purposes, we treat it as a plane ($x-y$ plane) in which eddy currents $\vec{J}$ will flow. It is the thin conducting sheet of material on which damping forces will be generated. The free charge distribution in the conductor is disturbed when it moves through the magnetic field thereby setting up eddy currents. Subsequently, the eddy currents interact with the static magnetic field creating magnetic forces that act on the conductor. Currents and forces induced due to the motion of the conductor through the magnetic field are commonly described using Lenz's law [2]:

> "If a current flows, it will be in such a direction that the magnetic field it produces tends to counteract the change in flux that induced the emf."

Magnetic forces $\vec{f}$ per unit volume acting on the conductor are given by the simple formula:

$$\vec{f} = \vec{J} \times \vec{B}. \tag{1}$$

Using Ohm's law, the current density is proportional to the driving force:

$$\vec{J} = \sigma \vec{v} \times \vec{B}. \tag{2}$$

where σ is the conductivity of the thin metal conductor, and $\vec{v}$ is the conductor velocity. For the simplified conditions we are considering here, Equations (1) and (2) used together

produce a formula for the force acting on the conductor that is qualitatively consistent with Lenz's law. The resulting formula is expressed as a function of the field strength B_z and conductor velocity $\vec{v} = v\hat{i}$

$$\vec{f} = -\sigma v {B_z}^2 \hat{i}. \tag{3}$$

The salient features of the above formula are its simplicity and qualitative correctness. We note that the body force direction is always the opposite of the velocity and secondly its magnitude is proportional to the magnitude of the velocity. In form, it looks like a linear viscous damping.

While the force formula in Eq. 3 is simple to use and qualitatively correct, it over-predicts the resulting magnetic force [7], [4]. An enhancement to the above model is to begin with the following formula for the electromotive force

$$\vec{J} = \sigma(\vec{E} + \vec{v} \times \vec{B}), \tag{4}$$

where $\vec{E}$ is the quasi-static electric field. Taking the curl of both sides and using vector identities we arrive at:

$$\nabla \times \vec{J} = -\sigma(\vec{v} \cdot \nabla)\vec{B} = \vec{\omega}. \tag{5}$$

Note the definition of $\vec{\omega}$ on the right hand side of Eq. (5). We will refer to it often throughout the development.

Since charge in the conductor is not expected to build up over time, conservation of charge dictates that the current $\vec{J}$ must be divergence free:

$$\nabla \cdot \vec{J} = 0. \tag{6}$$

Eqs. (5) and (6) are the starting point for the mathematical model that we will work with in this paper.

2 Mathematical Models

In this section we further develop the mathematical models used to describe eddy currents in the shuttle conductor as well as the magnetic fields that drive the eddy currents. In this analysis we assume that these problems are decoupled and solve first for the magnetic field and secondly for the eddy currents. We are ultimately interested in calculating the body forces that arise due to the eddy currents.

2.1 Eddy Currents

It is important that the mathematical model for Eqs. (5) and (6) address the divergence free condition on $\vec{J}$. Because the divergence of a curl is always zero, we choose $\vec{J}$ as:

$$\vec{J} = \nabla \times \vec{A}, \tag{7}$$

where $\vec{A}$ is a vector potential function. With this definition for $\vec{J}$, the divergence free condition is automatically satisfied. Substituting into (5) we get

$$\nabla \times (\nabla \times \vec{A}) = \vec{\omega}. \tag{8}$$

For this analysis, we assume that $B_z(x,y)$ is constant through the thickness of the conductor and that the in-plane components B_x and B_y are zero throughout the conductor. To arrive at the final form for $\vec{\omega}$ we take $\vec{v} = v\hat{i}$ for the conductor which leads to:

$$\vec{\omega}(x,y) = -\sigma v \frac{\partial B_z}{\partial x} \hat{k} = \omega_z \hat{k}. \tag{9}$$

Using our assumptions that $\vec{\omega}$ is independent of z and only has a $\hat{k}$ component, Eq. (8) reduces to a 2 dimensional scalar Poisson equation [3] for the z-component of $\vec{A}$:

$$-\nabla^2 A_z = \omega_z. \tag{10}$$

To complete the model we must consider the boundary conditions for A_z. Charge is constrained to the conductor and this leads the following condition on $\vec{J}$ at the conductor boundary:

$$\vec{J} \cdot \vec{n} = 0, \tag{11}$$

where $\vec{n}$ is the unit normal to the conductor boundary. Substituting Eq. 7 into Eq. 11 gives

$$0 = (\nabla \times A_z \hat{k}) \cdot \hat{n}. \tag{12}$$

For the problems considered here, which consist of rectangular domains, it is not difficult to see that setting $A_z(x,y) = 0$ for (x,y) on the boundary will satisfy Eq. 12.

2.2 Magnetic Field

As the shuttle conductor moves in the static magnetic field, eddy currents are induced according to Lenz's law. Thus we must calculate the magnetic field in the shuttle conductor. The governing equation for magnetostatics is given by:

$$\nabla \cdot \vec{B} = 0 \tag{13}$$

We assume a linear constitutive law for $\vec{B}$ as given by:

$$\vec{B} = \mu \vec{H} \tag{14}$$

where μ is the magnetic permeability of the medium and $\vec{H}$ is just "**H**" (apparently $\vec{H}$ has historically had no sensible name [2] page 260). For purposes of modeling permanent magnets, the above relation can be written as:

$$\vec{B} = \mu_0(\vec{H} + \vec{M}), \tag{15}$$

where $\mu_0 = 4\pi \times 10^{-7}\ N/A^2$ is the permeability of free space and $\vec{M}$ is the magnetization vector of the permanent magnet. At material boundaries the normal component of the magnetic field is required to be continuous. This is expressed mathematically using the jump bracket notation $[\vec{B} \cdot \hat{n}] = 0$ where $\hat{n}$ is the unit normal to the material interface. In the far field it is assumed that $\vec{B} = \vec{0}$.

3 Finite Element Formulation

In this section we develop and discuss the finite element models for both the magnetic field and eddy current calculations.

3.1 Magnetic Field

For problems in which there are multiple materials, the magnetic field is at best piecewise continous. This is a direct result of the jump conditions that $\vec{B}$ must satisfy at material interfaces. In subregions of the computational domain where there is only one material the magnetic field is smooth. These facts are crucial to the finite element formulation for the magnetic field. For smooth subregions, the following formula is convenient for deriving the finite element weak form for the magnetic field:

$$\nabla \cdot (\phi \vec{B}) = \phi \nabla \cdot \vec{B} + \vec{B} \cdot \nabla \phi, \tag{16}$$

where ϕ is a smooth function. Applying the divergence theorem to the left hand side and rearranging we get:

$$0 = \int_{\Omega_s} \phi \nabla \cdot \vec{B} = -\int_{\Omega_s} \vec{B} \cdot \nabla \phi + \int_{\partial \Omega_s} \phi \vec{B} \cdot \hat{n} \tag{17}$$

where Ω_s is the smooth subregion with boundary $\partial \Omega_s$. We can extend the above result to the entire computational domain by utilizing the jump conditions on $\vec{B}$ at material interfaces. Finally, we we eliminate the second integral on the right hand side by choosing test functions ϕ that vanish on the boundary. Dropping the subscript on the domain Ω we are left with:

$$0 = \int_{\Omega} \vec{B} \cdot \nabla \phi \tag{18}$$

A function $\vec{B}$ that satisfies Eq. (18) is divergence free in the weak sense. Only a minimal amount of regularity is required from ϕ – it must only have a gradient that is square-integrable. This facilitates the use of piecewise polynomials as is typical in finite element formulations.

In order to proceed with the finite element model, we substitute the constitutive Eq. (15) into Eq. (18):

$$0 = \int_{\Omega} (\vec{H} + \vec{M}) \cdot \nabla \phi \tag{19}$$

With the assumption that there are no source currents and that the eddy currents are uncoupled from the static magnetic field, a scalar potential ψ may be utilized to define $\vec{H}$:

$$\vec{H} = -\nabla \psi \tag{20}$$

The magnetization $\vec{M}$ is given data and the scalar potential ψ is the unknown and our primary variable. With these definitions, we are now ready to define the space of functions from which we seek the finite element solution for ψ:

$$H_0(\Omega) = \{\phi : \nabla \phi \in L_2(\Omega),\ \phi = 0 \ on\ \Gamma\} \tag{21}$$

where $L_2(\Omega)$ is the set of square-integrable functions. Substituting Eqs. (15) and (20) into Eq. (18), we define the following formal problem for determining the scalar potential ψ:

find $\psi \in H_0(\Omega)$ such that

$$A(\psi, \phi) = g(\phi) \ \forall \ \phi \in H_0(\Omega), \tag{22}$$

where $A(\psi, \phi)$ and $g(\phi)$ are bilinear and linear forms defined as:

$$A(\psi, \phi) = \int_\Omega \mu_0 \mu_r \nabla\phi \cdot \nabla\psi, \tag{23}$$

$$g = \mu_0 \int_{\Omega_e} \vec{M} \cdot \nabla\phi_j. \tag{24}$$

and μ_r is the relative permeability of the medium. Note that the magnetization vector $\vec{M}$ is a known quantity and gives rise to the source term. It is also important to note that $\vec{M}$ and μ_r depend upon position. For example, when the region of integration is over a magnet, $\vec{M}$ is nonzero and $\mu_r = 1$ whereas over a piece of iron $\vec{M} = 0$ and $\mu_r = \mu_{fe}/\mu_0$ where μ_{fe} is the permeability of iron.

In the finite element method [6], we break up the computational domain into pieces (finite elements). Over a finite element, the scalar potential function ψ is approximated by a set of polynomials:

$$\psi^e = \sum_{i=1}^{N} \psi_i \phi_i^e(\xi, \eta), \tag{25}$$

where $\phi_i^e(\xi, \eta)$ are the local element shape functions and N is the number of shape functions utilized on the element. The scalar values ψ_i are the unknown degrees of freedom in the problem.

While the formulation described here is suitable for most element types and applies to 3 dimensions, we implemented the 2 dimensional rectangles as shown in Figure 1. In this case we used linear interpolation as follows (one for each vertex of the rectangle):

$$\begin{aligned}
\phi_1^e(\xi, \eta) &= (1 - \frac{\xi}{a})(1 - \frac{\eta}{b}), \\
\phi_2^e(\xi, \eta) &= \frac{\xi}{a}(1 - \frac{\eta}{b}), \\
\phi_3^e(\xi, \eta) &= \frac{\xi\eta}{ab}, \\
\phi_4^e(\xi, \eta) &= (1 - \frac{\xi}{a})\frac{\eta}{b}.
\end{aligned} \tag{26}$$

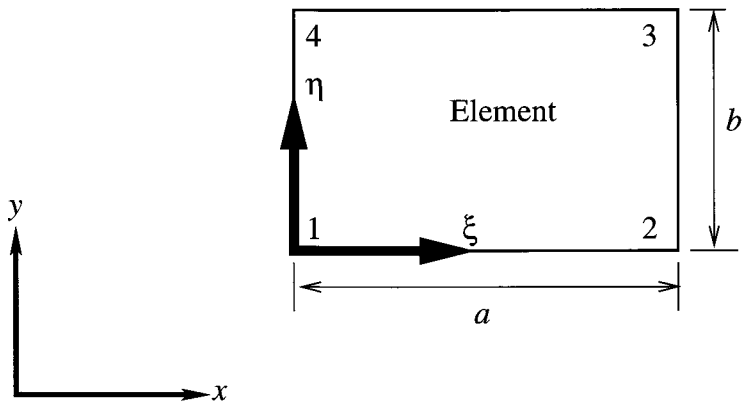

Figure 1. Rectangle finite element shape functions

In the finite element method, it is typical that the test functions ϕ are the same as those used to interpolate the primary variable ψ. Substituting the element level interpolation for ψ given in Eqs. (26) into Eq. (23) and performing the integration yields the following element stiffness matrix:

$$A^e = A^{xe} + A^{ye}, \tag{27}$$

where

$$A^{xe} = \frac{\mu_0 \mu_r b}{6a} \begin{pmatrix} 2 & -2 & -1 & 1 \\ -2 & 2 & 1 & -1 \\ -1 & 1 & 2 & -2 \\ 1 & -1 & -2 & 2 \end{pmatrix} \text{ and } A^{ye} = \frac{\mu_0 \mu_r a}{6b} \begin{pmatrix} 2 & 1 & -1 & -2 \\ 1 & 2 & -2 & -1 \\ -1 & -2 & 2 & 1 \\ -2 & -1 & 1 & 2 \end{pmatrix}. \tag{28}$$

Similarly, we can evaluate the right hand side by substituting Eqs. (26) into Eq. (24) and performing the integations to yield the element level source terms:

$$g^e = \frac{\mu_0}{2} \begin{pmatrix} -bM_x - aM_y \\ bM_x - aM_y \\ bM_x + aM_y \\ -bM_x + aM_y \end{pmatrix}. \tag{29}$$

Again it is important to note that this integral is only evaluated over elements which have a remnant magnetization vector $\vec{M} = M_x \hat{i} + M_y \hat{j}$.

3.2 Eddy Currents

In a practical sense the mathematical models for the eddy currents and the magnetic field are nearly identical. By integrating Eq. (10) by parts and applying the homogeneous boundary condition on A_z, the following formal weak problem is given: find $A_z \in H_0(\Omega)$ such that

$$C(A_z, \phi) = g(\phi) \ \forall \ \phi \in H_0(\Omega) \tag{30}$$

where $C(A_z, \phi)$ and $h(\phi)$ are bilinear and linear forms defined as:

$$C(A_z, \phi) = \int_\Omega \nabla A_z \cdot \nabla \phi \tag{31}$$

$$h(\phi) = \int_\Omega \omega_z \phi \tag{32}$$

By setting $\mu_0 \mu_r = 1$, we can re-use the element stiffness matrices given in Eq. (28).

It is important to note that Ω for the magnetic field and the eddy currents calculations are different. They have a non trivial intersection but with our assumptions and approximations they are different. We will discuss this topic in the next section.

While the bilinear forms are nearly identical it is the interpretation and application of the primary variables that are fundamentally different. We note that $\vec{H}$ is derived from the primary variable through the gradient operator while the $\vec{J}$ is derived by taking the curl of the vector potential.

4 Modeling a Device

In this section we discuss the application of the above mathematical models for calculating the damping forces acting on mechanical oscillators similar to that shown in Figure 2. The device consists of a relatively thin sheet of metal (shuttle conductor), a set of tethering flexure springs, and sets of magnet pairs (only 1 pair of magnets shown in figure). Each pair of magnets is configured so that one magnet is above the shuttle conductor and one is below. The magnetization vector for each magnet within a pair is the same and is either along the $+z$ or $-z$ axes. For clarity, two pairs of magnets and their magnetization vectors relative to the global coordinate system are shown in Figure 3. Additional pairs are added along the length of the shuttle (along the x axis) with their magnetization vector oriented in the opposite direction from adjacent pairs. In this way the magnets work together to strengthen the magnetic field and its gradient along the x direction within the shuttle (note the definition of ω_z given in Eq. (9).

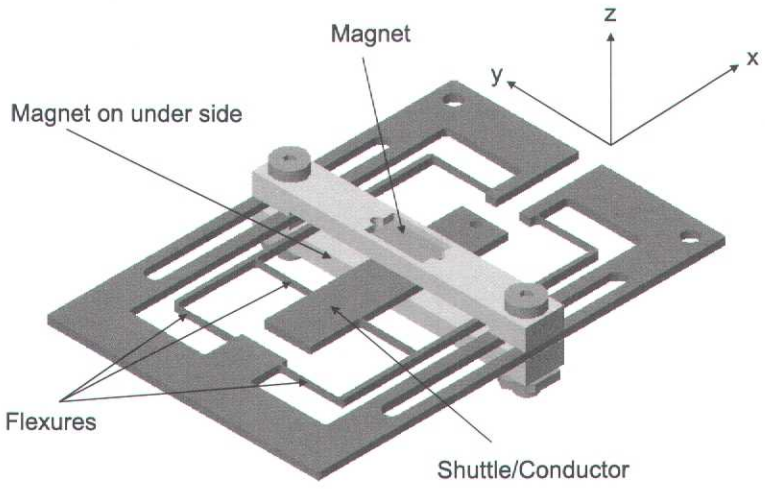

Figure 2. Damped Oscillator Schematic

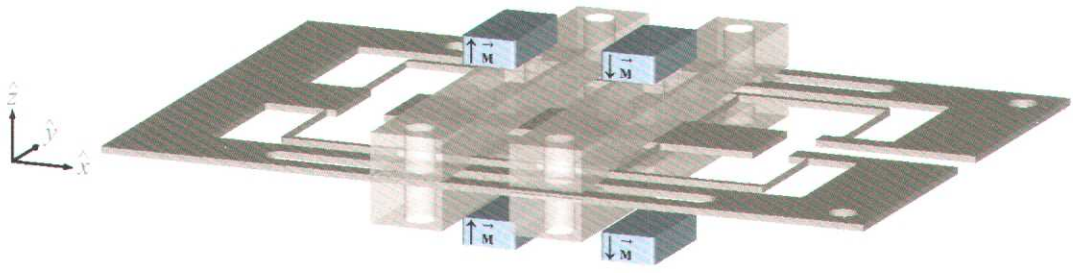

Figure 3. Exploded View of Magnet Pairs (and magnetization) in Device

4.1 Magnetic Field

Using the finite element models above, we first solve the problem defined by Eq. (22) for ψ in the $x-z$ plane. Typical results for the magnetic field are shown in Figure 4. Note the direction of the field vectors (depicted in blue) in the shuttle conductor (depicted in red). Purposefully, the shuttle conductor is centered between pairs of magnets, as shown in Figures (2) and (4), so that there is only one non-zero component of the magnetic field $\vec{B}(x,z=0) = B_z(x)\hat{z}$ at $z=0$. In this way we satisfy one of our modeling assumptions (see discussion leading to Eq. 9) for the eddy current analysis. Also note the variation of the magnetic field within the shuttle as shown in the lower plot of Figure 4.

4.2 Eddy Currents

The shuttle conductor exists in the $x-y$ plane and we assume that the magnets are sufficiently long (in the y direction) compared to the y width of the shuttle conductor so that the magnetic fields calculated can be assumed to be independent of y. For the eddy current and force calculations, we must calculate the magnetic field within the shuttle conductor at $z=0$. The shuttle conductor is not a magnetic material and has a relative permeability of $\mu_r = 1$. Using this fact and the definition for $\vec{H}$ in Eq. (20) and the interpolation functions for ψ in Eq. (25), the z-component of the magnetic field in an element is given as:

$$B_z(x) = -(b_1\alpha_1(x) + b_2\alpha_2(x)), \tag{33}$$

where $\alpha_1(x)$, $\alpha_2(x)$, b_1 and b_2 are defined by:

$$\begin{aligned} \alpha_1(x) &= 1 - x/a, \\ \alpha_2(x) &= x/a, \\ b_1 &= \mu_0 \frac{\psi_4 - \psi_1}{b_z}, \\ b_2 &= \mu_0 \frac{\psi_3 - \psi_2}{b_z}, \end{aligned} \tag{34}$$

These equations are particularly useful for calculating ω_z defined in Eq. (9).

$$\omega_z = \frac{\sigma v}{a}(b_2 - b_1). \tag{35}$$

We note that it is ω_z that drives the eddy currents and that ω_z is a linear function of the conductor velocity and depends upon the gradient of the magnetic field. This fact is crucial for calculating a damping coefficient described in the next section. Because ω_z is constant

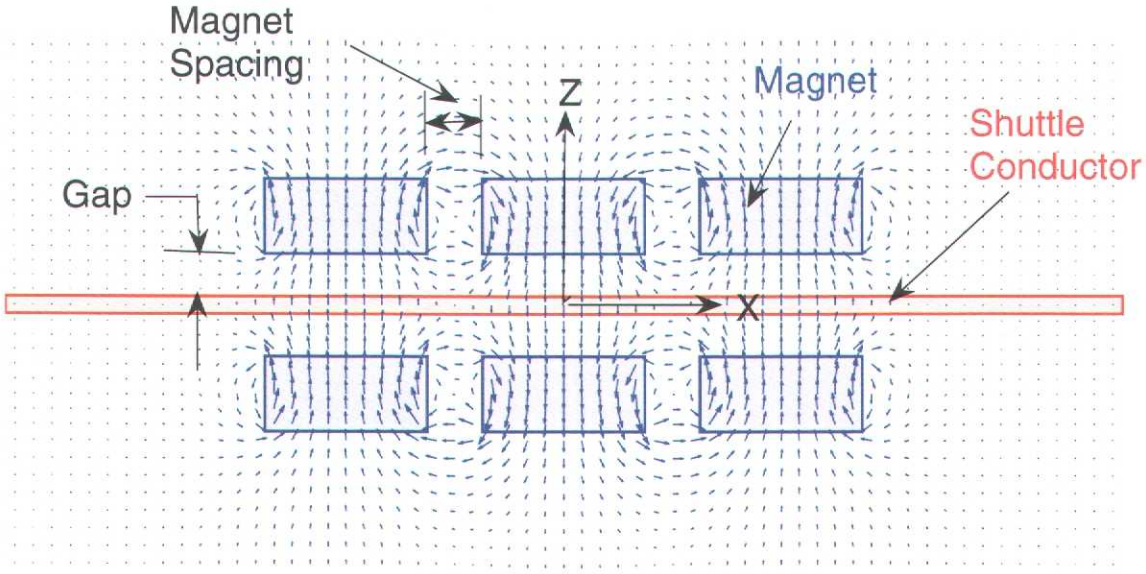

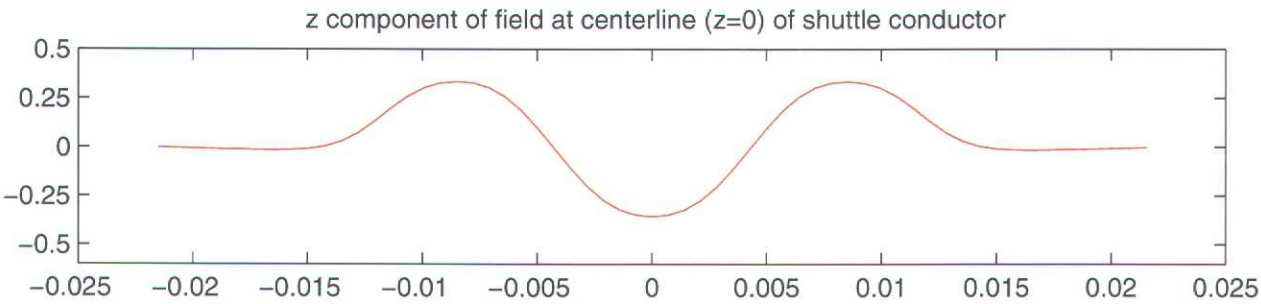

Figure 4. Magnetic field ($x-z$ plane): Shuttle conductor centered between 3 magnet pairs

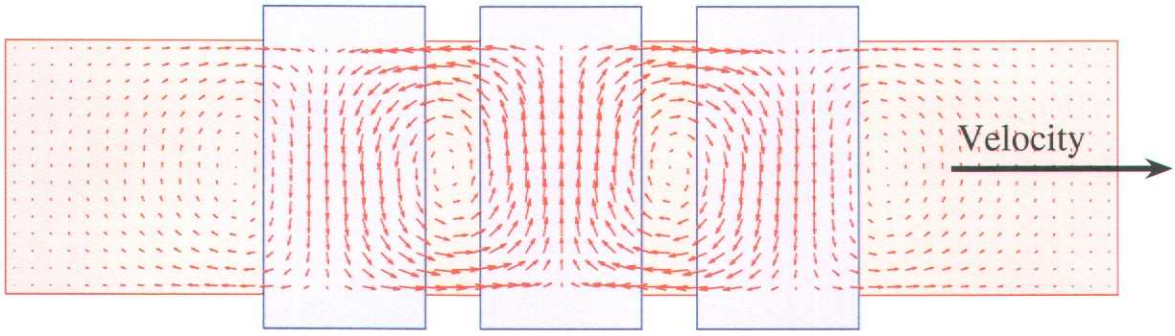

Figure 5. Current $\vec{J}$ in $y-z$ plane: Magnets in blue overlay with $\vec{J}$ values plotted at the element centroids

over an element, the integral given in Eq. (32) which defines the right-hand side source term for the eddy current problem, is easily evaluated on an element:

$$h^e(\phi_i) = \frac{\omega_z ab}{4}\begin{pmatrix}1\\1\\1\\1\end{pmatrix}. \tag{36}$$

Results from an eddy current calculation are shown in Figure 5. These results correspond with the magnetic field shown in Figure 4.

An important verification is that the model correctly predicts no current if the gradient of the magnetic field is zero. For example, if one large magnet pair completely covered the shuttle conductor so that there is no variation in the magnetic field within the conductor, then only Hall voltages would be produced if the conductor were to move. Setting $\vec{J}=0$ in Eq. (4) one can find the Hall field $\vec{E} = -\vec{v}\times\vec{B}$.

4.3 Calculating Damping Forces

In this analysis we are primarily interested in calculating the forces induced due to the interaction of the eddy currents $\vec{J}$ with the magnetic field $\vec{B}$. Using Eq. (1) the calculation is a post-processing step conducted after both the magnetic field and the eddy currents are known. In view of Eq. (35), it is obvious that the eddy currents $\vec{J}$ are proportional to the

shuttle conductor velocity. Therefore define a new vector $\vec{J}$ by writing $\vec{J}$ as:

$$\vec{J} = v\vec{J} \tag{37}$$

We are interested in measuring the amount of eddy current damping induced for a second order spring-mass system:

$$M\ddot{x} + Kx = F_x, \tag{38}$$

where F_x is the damping force in the x direction, M is the shuttle conductor mass, and K is the linear flexure spring stiffness of the oscillator shown in Figure 2. To calculate F_x we substitute Eq. (37) into Eq. (1) to arrive at a damping force per unit volume:

$$\vec{f} = f_x\hat{i} + f_y\hat{j} = (\vec{J} \times \vec{B})v. \tag{39}$$

Finally, F_x is found by integrating over the shuttle conductor volume:

$$\vec{F} = F_x\hat{i} + F_y\hat{j} = \int_\Omega f_x\hat{i} + f_y\hat{j} = v\int_\Omega \vec{J} \times \vec{B}. \tag{40}$$

The net force acting on the shuttle is exactly the opposite direction of the shuttle velocity. As previously indicated, the shuttle conductor is constrained to move along the x axis with velocity v, and therefore the net force on the shuttle becomes:

$$\vec{F} = F_x\hat{i} + 0\hat{j} = v\int_\Omega \vec{J} \times \vec{B} = -Cv\hat{i}, \tag{41}$$

where we identify the familar damping coefficient C and also the shuttle velocity $v = \dot{x}$. For later reporting we also identify the damping ratio ζ as

$$\zeta = \frac{C}{2M\omega_n} \text{ where } \omega_n^2 = \frac{K}{M}. \tag{42}$$

To facilitate the calculation of C, recall the definition for $\vec{J}$ in Eq. (7) as well as the interpolation functions used for A_z given in Eq. (26). Using these definitions we evaluate the integral for C on an element by element basis.

$$c_{ex}\hat{i} + c_{ey}\hat{j} = -\int_{\Omega_e} \vec{J} \times \vec{B}, \tag{43}$$

where

$$
\begin{aligned}
c_{ex} &= \frac{ab(b_1+b_2)(j_{21}+j_{22})}{4}, \\
c_{ey} &= \frac{ab(b_1(2j_{11}+j_{12})+b_2(j_{11}+2j_{12}))}{6},
\end{aligned} \tag{44}
$$

and $j_{11}, j_{12}, j_{21}, j_{22}$ are defined as:

$$
\begin{aligned}
j_{11} &= \frac{A_{z4}-A_{z1}}{b}, \\
j_{12} &= \frac{A_{z3}-A_{z2}}{b}, \\
j_{21} &= \frac{A_{z2}-A_{z1}}{a}, \\
j_{22} &= \frac{A_{z3}-A_{z4}}{a}.
\end{aligned} \tag{45}
$$

The damping coefficient C is obtained by summing over all elements:

$$
C = t\sum_{e}^{N_e} c_{ex}, \quad 0 = t\sum_{e}^{N_e} c_{ey}. \tag{46}
$$

where t is the thickness of the shuttle conductor and N_e is the number of elements in the mesh. Corresponding with Figures 4 and 5, the body force distribution in the shuttle conductor is shown in Figure 6. It is worth noting that one can visually see a net force along the $-x$ axis. In contrast the net y component of the force is zero ($f_y(y) = -f_y(-y)$).

4.4 Sensitivity Analysis

Using the models described above, sensitivity studies were conducted in order to identify critical design parameters and investigate how magnetization, magnet spacing, and gap may affect the damping ratio. Design variables are annotated in Figure 5. The spider plot shown in Figure 7 compares the effects of modifying individual design parameters and material properties. The y-axis is the predicted damping ratio ζ (see Eq. (42))described in the previous section. In order to make comparisons when modifying parameters that have different units or scales, the x-axis is normalized such that 0 corresponds to the nominal value and the difference between the maximum and minimum values is 2. Bounds on parameters can either represent the design space or uncertainties (see Wittwer, [9], page 118) and Figure 7 is a combination of both. We note that this sensivity analysis does not show all possible parameter variations. Of those shown, the magnet spacing, gap and beam width are design parameters, while resistivity is a property of the shuttle conductor, and magnetization is a property of the given magnets.

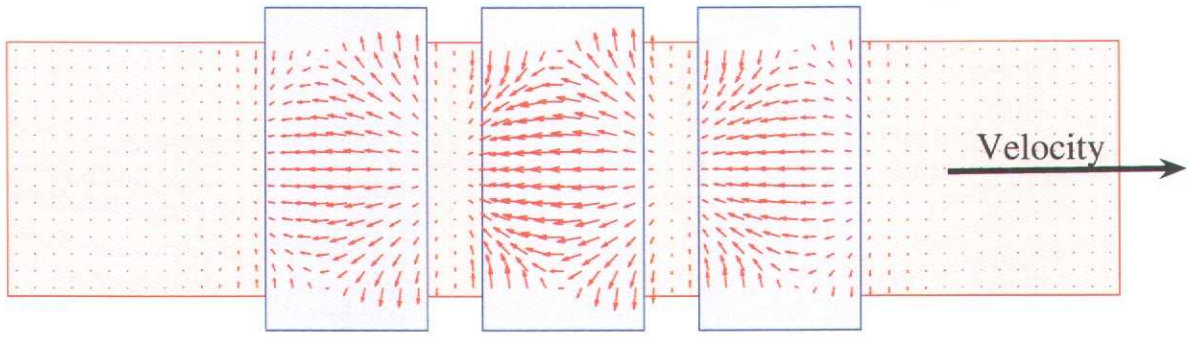

Figure 6. Magnetic body force distribution

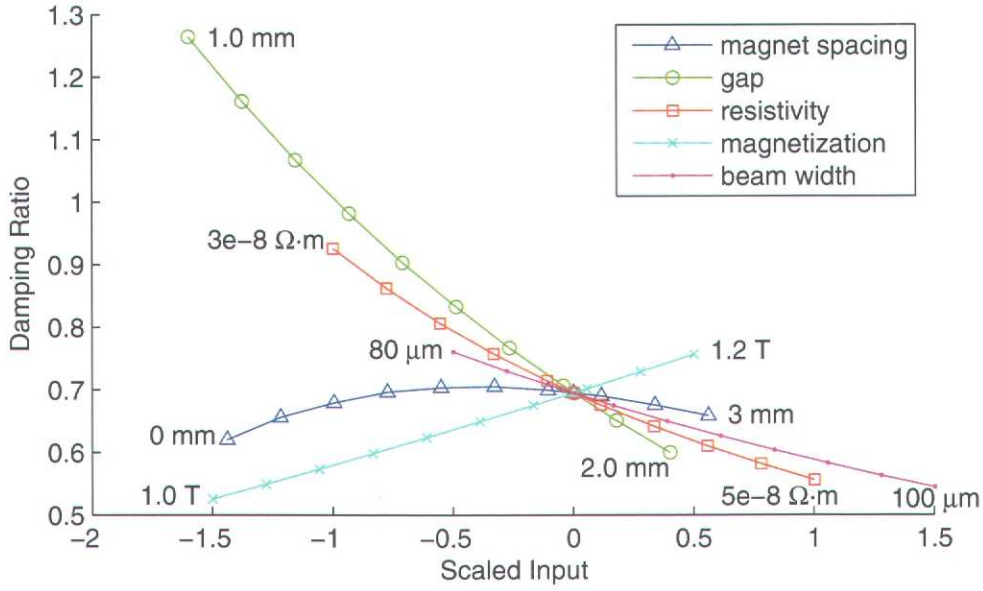

Figure 7. Damping ratio sensitivities: magnet spacing, gap, resistivity, magnetization, beam width

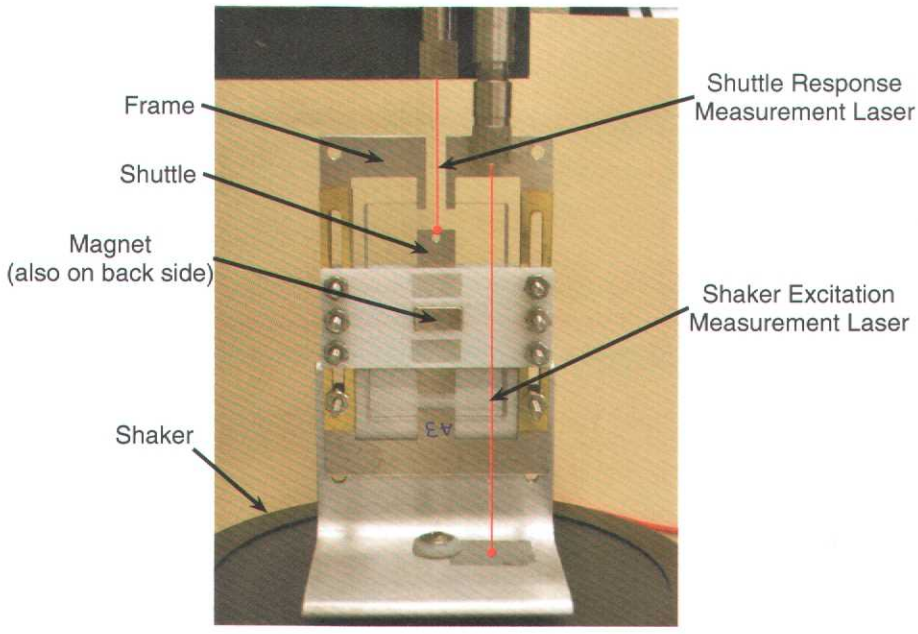

Figure 8. Picture of the test setup

5 Correlation with Measurements

5.1 Experimental Setup and Measurement Results

To demonstrate the effectiveness of eddy current damping and validate the modeling, several prototype devices (as shown in Figure 2) were fabricated. These devices were designed with the facility for adjusting eddy current damping by adding or removing a number of small magnets.

As shown in Figure 8, the devices were mounted with an adapter to a B&K 4809 shaker for testing to quantify the damping generated. To measure the motion of the moving parts relative to the input motion from the shaker, two laser Doppler velocimeters (LDVs) were used. A pseudo-random voltage signal bandlimited from 10 Hz to 210 Hz was used to drive the shaker motion. The velocity of the shaker input and the velocity of the shuttle mass on the demonstration part were measured independently with the two LDVs. The ratio of the two measurements gives a frequency domain estimate for the transmissibility from the shaker input to the shuttle. The excitation was kept low to ensure linearity of the vibrations and to prevent damage to the part if sharp resonances occurred. The first test was conducted without any magnets on the demonstration part as a baseline to determine the structural damping.

Two sets of tests were conducted – one set with magnets only (see Figure 4) and the

Number of Magnet Pairs	Natural Frequency (Hz)	Damping Ratio
0	28.1	0.0002
1	27.6	.10
2	27.2	.21
3	27.9	.46
4	31.0	.62
5	31.4	.73

Table 1. Curve-fitting results for demonstration tests

second with magnets and a backing plane as shown in Figure 9. Note the increased magnetic field strength in the shuttle when the backplane is utilized. The backing plane is a magnetic shields for space outside the shuttle package and enhances the strength of the magnetic field in the shuttle by directing the field lines of the individual magnets to more effectively work together.

Results for these tests are shown in Figures 10 and 11. The frequency response of the device is included only up to 50 Hz in order to capture the first resonance only. This resonance, at 28 Hz, is the translation of the shuttle in the direction of excitation. This is the motion that we are modeling and intending to dampen via magnetic forces. As magnets are added the damping ratio increases significantly and with the addition of the backing plate the damping ratio increases beyond a value of $\zeta = 1.0$ (critical damping).

A linear second order curve-fit [5] (see the Appendix section for additional details) of the region near the first resonance was used to identify the natural frequency and damping ratio for each case. This data is reported in Tables 1 and 2. Damping ratios are written as a fraction of critical damping. As shown in Table 1 and Figure 10, there is very little damping without magnets. With the addition of just one pair of magnets, damping is increased significantly. With each additional pair of magnets the data shows increased levels of damping although the increase is not as significant as that seen with the first pair. The addition of the backing plate drives the damping even higher. Table 2 shows damping values for cases with the backing plate. Once the damping ratio goes beyond 1.0, roots of the second-order curve-fit of the resonance cease to be complex but we continue to treat it as though it is complex to be consistent in our comparisons.

We finally note that the reported natural frequency ω_n tends to increase with increasing levels of damping. At this time we do not have an explanation for this.

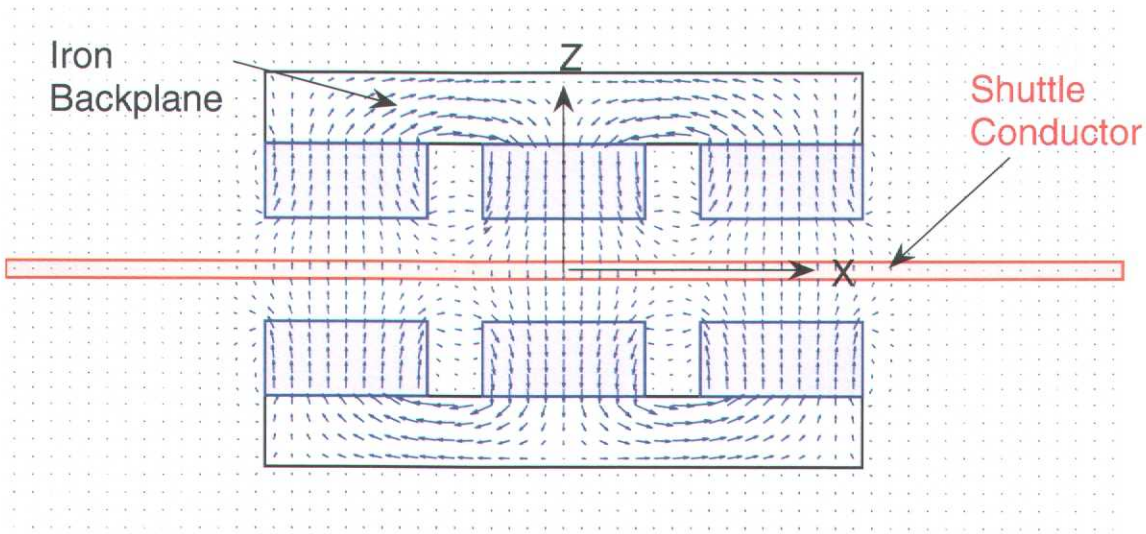

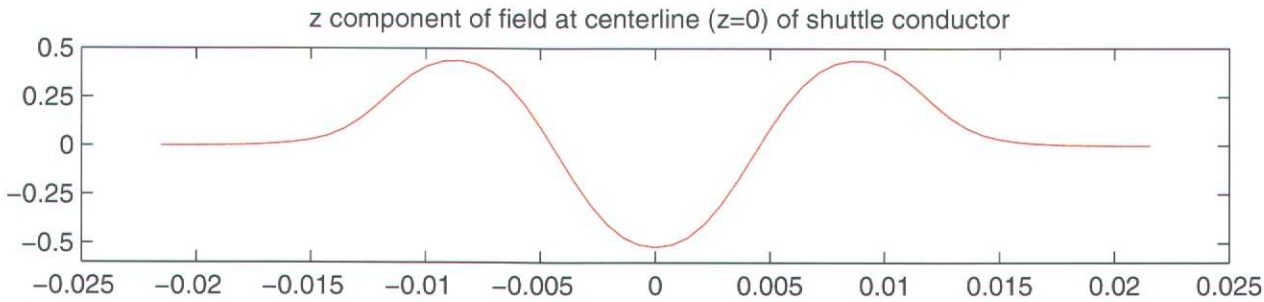

Figure 9. Magnetic field in (x-z plane) enhanced by backplane: Shuttle conductor centered between 3 magnet pairs

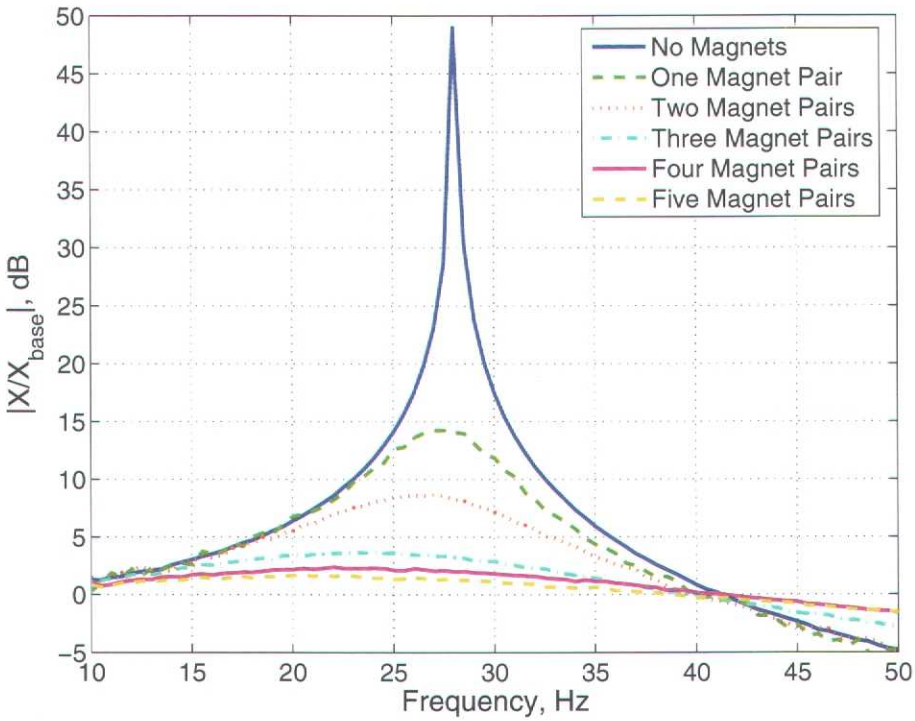

Figure 10. Transmissibility measurements for eddy current demonstration without backing plate

Number of Magnet Pairs	Natural Frequency (Hz)	Damping Ratio
2	29.7	.55
3	29.5	.84
4	33.0	1.05
5	32.8	1.25

Table 2. Curve-fitting results for demonstration tests with a backing plate

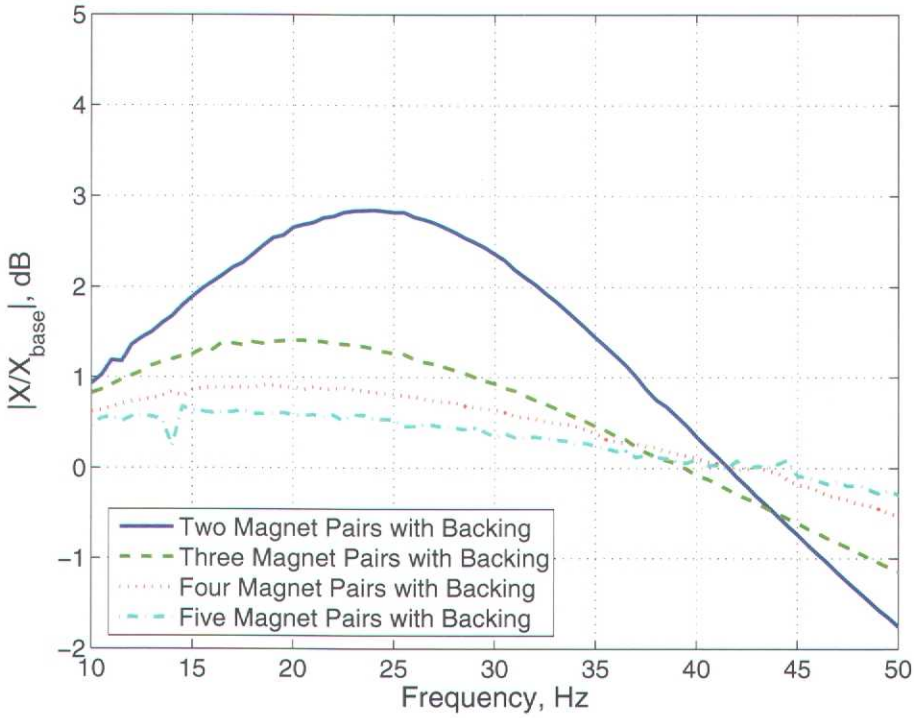

Figure 11. Transmissibility measurements for eddy current demonstration with a backing plate

Variable	Units	Value
Gap	mm	1.8 ± 0.08
Resistivity	$\Omega - m$	$4e-8 \pm 0.3e-8$
Magnetization	Tesla	1.15 ± 0.05
Beam Width	μm	85 ± 5

Table 3. Uncertainty analysis input data

5.2 Model Validation

To compare experimental results to the model, it is necessary to take into account uncertainties in the input data. Here we have included magnetization, resistivity, beam width, and other values that were found to be important factors from the sensitivity study. Table 3 lists the values and uncertainties used in the simulation-based uncertainty analysis.

Recall that the modeled damping ratio is calculated using Eq. (42) which depends directly upon the flexure stiffnesses of the tethering springs (as shown in Figure 2) through the natural frequency ω_n. For the simulation, a natural frequency of 30.8 Hz was calculated as in [8] using

$$K = \frac{2Etw^3}{L^3}, \tag{47}$$

where E is young's modulus, t is the shuttle thickness, w is the flexure width, and L is the length of the flexures. Note that the damped oscillator shown in Figure 2 is monolithic (i.e. fabricated from a single layer of material). The beam width w is crucial to the stiffness calculation since the stiffness depends cubicly on this parameter. Beams widths were measured using a scanning electron microscope.

The analysis was performed using a second-order surrogate-based Monte Carlo method [9]. This approach first creates a multi-dimensional second-order response surface for the domain represented by the uncertainties in Table 3. This surrogate model is then used in a Monte Carlo simulation consisting of 10000 function evaluations, where the uncertainties are independent uniform distributions. The resulting mean, standard deviation, and 95% intervals for the predicted damping ratio are reported in Tables 4 and 5.

The results of the simulation-based uncertainty analysis show that the model is consistently predicting a damping ratio higher than the measured value (see Figure 12). In some cases, the measured value falls within the 95% intervals. Although the model is showing some bias, the trends shown in Figure 12 are in good agreement.

The fact that some of the measurements lie outside of the 95% intervals indicates that the given uncertainties alone do not account for the observed model bias. More work is

	Measured	Model		
Magnet Pairs	ζ	ζ	StDev	95% Interval
1	0.1	0.15	0.014	[0.13,0.18]
2	0.21	0.31	0.028	[0.26,0.37]
3	0.46	0.51	0.046	[0.43,0.61]
4	0.62	0.70	0.064	[0.59,0.84]
5	0.73	0.88	0.080	[0.73,1.04]

Table 4. Measured and calculated ζ: uncertainty analysis results (no back plate)

	Measured	Model		
Magnet Pairs	ζ	ζ	StDev	95% Interval
2	0.55	0.60	0.054	[0.50,0.71]
3	0.84	0.93	0.084	[0.77.1.10]
4	1.05	1.29	0.116	[1.08,1.53]
5	1.25	1.57	0.143	[1.31,1.86]

Table 5. Uncertainty Analysis Results (with backplane)

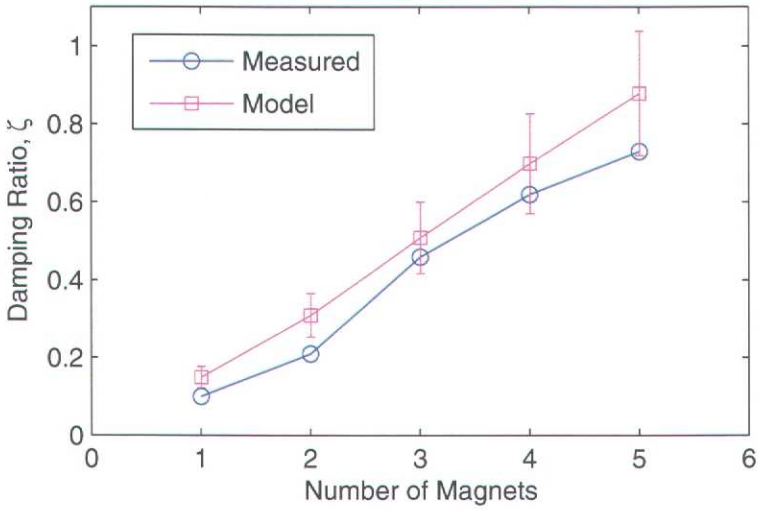

Figure 12. Uncertainty Analysis: 95 % Confidence Bands on damping ratio

required to determine what is causing the difference between the model and the measurements. The assumption that the magnetic field is completely 2-dimensional may be one source of this bias. At the ends of the magnets, the fields are actually 3-dimensional, so our model will over-predict the strength of the field and subsequently over-predict the damping forces and coeffient. This hypothesis is supported by the data because as the number of magnets increases the model overpredicts the measured data by an increasing amount. Modeling the 3-dimensional magnetic field would likely lead to more accurate results.

The uncertainty contributions associated with Figure 4 are depicted in the pie chart Figure 13. This first order sensitivity analysis (based upon numerical calculation of first-order sensitivities) shows that all of the uncertainties included in the simulation have a significant effect on the damping ratio.

6 Conclusions

In this paper we presented mathematical and numerical models for two dimensional quasi-static eddy currents in a thin conducting sheet. Using the models, we reported the results of design sensitivity and model based uncertainty analyses. To validate the models we reported on damping measurements using Laser Dopler Velocimeters. Although analyses showed that there was some bias, possibly due to three dimensional magnetic field effects not included in the model, there was good correlation of the model with experimental data. It was shown that the model is useful for predicting eddy current damping forces.

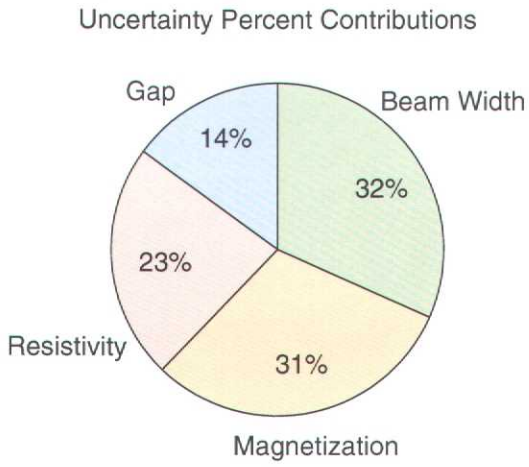

Figure 13. Uncertainty contributions to damping ratio

Based upon the results and analysis in this paper we conclude that using a 2-d magnetic field over predicts the magnetic forces near the ends of the magnets and thus over predicts the damping coefficient. As shown by the data and analysis, this effect increases with increasing number of magnets. Using a 3-d magnetic field in the model would tend to increase the correlation of the measured damping coefficients with those predicted by the model.

References

[1] H. W. Coleman and W. G. Steele. *Experimentation and Uncertainty Analysis for Engineers*. John Wiley & Sons, Inc., 2nd edition, 1999.

[2] David J. Griffiths. *Introduction to Electrodynamics*. Prentice Hall, New Jersey, 2nd edition, 1989.

[3] Jianming Jin. *The Finite Element Method in Electromagnetics*. Wiley, 1st edition, 2002.

[4] J. D. Kotulski. Magnetic forces on conductor moving in a magnetic field. Sandia National Laboratories unclassified memorandum to John Mitchell, October 2004.

[5] Nuno M. M. Maia and Julio M. M. Silva. *Theoretical and Experimental Modal Analysis*. Research Studies Press LTD., England, 1st edition, 1998.

[6] J. N. Reddy. *Applied Functional Analysis and Variational Methods in Engineering*. Mc-Graw Hill, 1st edition, 1986.

[7] P. J. Salzman, John Robert Burke, and Susan M. Lea. The effect of electric fields in a classic introductory physics treatment of eddy current forces. *American Journal of Physics*, 69(5):586–590, May 2001.

[8] Danelle M. Tanner, Albert C. Owen, and Fredd Rodriguez. Resonant frequency method for monitoring mems fabrication. In *SPIE's Proceedings*, volume 4980 of *Reliability, Testing, and Characterization of MEMS/MOEMS*, pages 220–228, January 2003.

[9] J. W. Wittwer. *Simulation-Based Design Under Uncertainty for Compliant Microelectromechanical Systems*. PhD thesis, Brigham Young University, 2005.

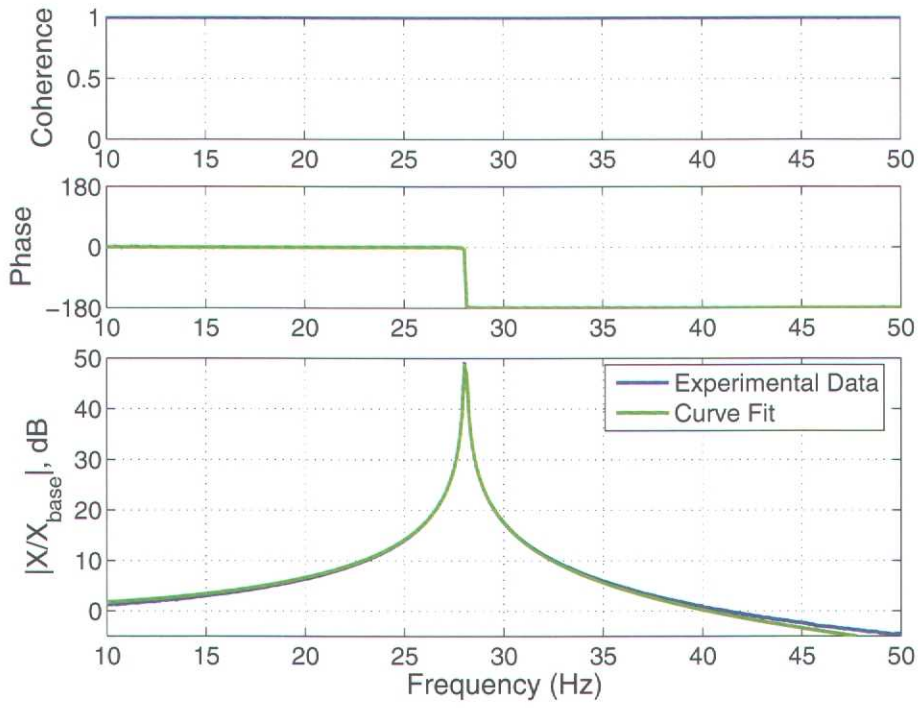

Figure A.1. Comparison of Experimental Data and Analytical Curve Fit for the No Magnets Case

A Frequency Response Curve Fitting

A linear second order curve-fit of the first resonance was used to identify the resonant frequency and damping for each case. The data collected was transmissibility and the single degree of freedom transmissibility in the Laplace domain has the form

$$H(s) = \frac{b_1 s + b_0}{s^2 + a_1 s + a_0}. \tag{48}$$

where $a_1 = 2\zeta\omega_n$ and $a_0 = \omega_n^2$. The vaiables b_1 and b_0 do not directly affect the resonant frequency and damping that we are looking for. All of these variables are determined using a least squares fit to the experimental data. Figures A.1, A.2, and A.3 show three example data sets curve fit using this method. In all cases the fit close to the peak amplitude is very good. The deviation of the curve fit from the experimental data at higher frequencies is due to unmodeled dynamics at higher frequencies.

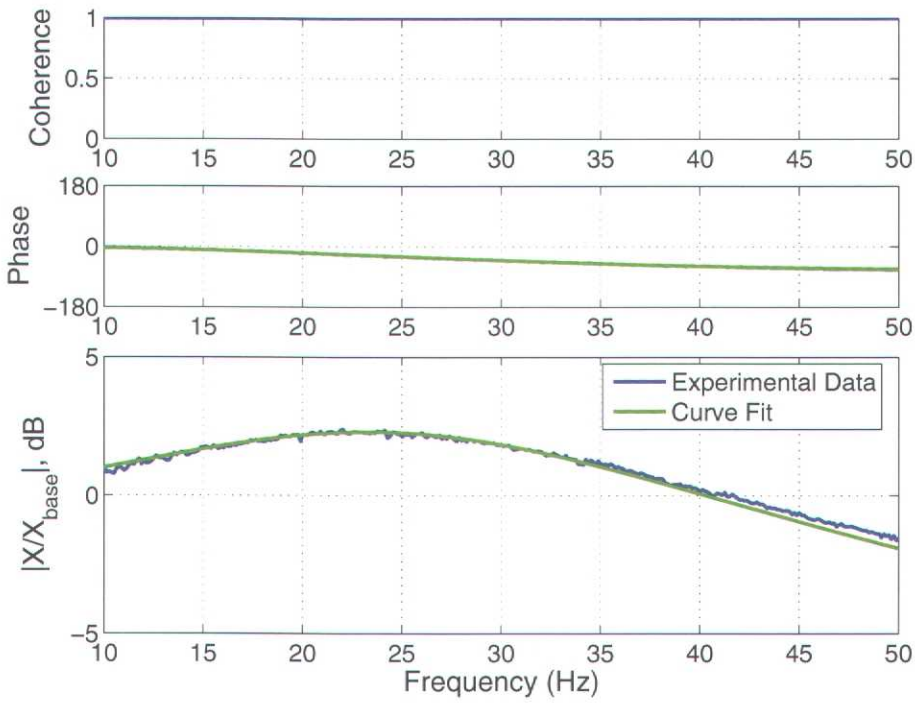

Figure A.2. Comparison of Experimental Data and Analytical Curve Fit for the Four Magnets Case

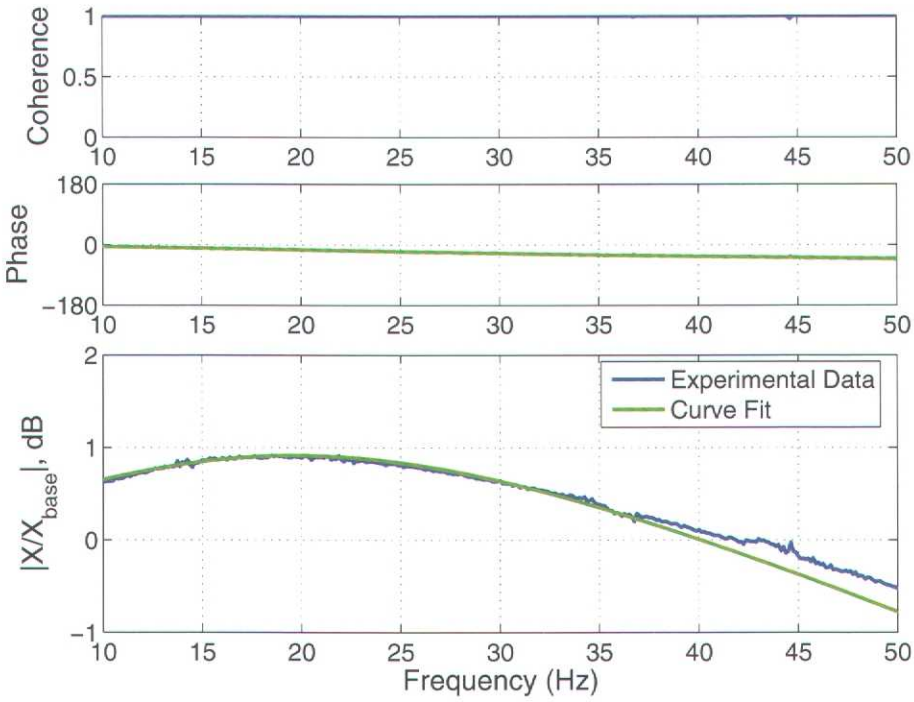

Figure A.3. Comparison of Experimental Data and Analytical Curve Fit for the Four Magnets Case with a Backing Plate

DISTRIBUTION:

1 Professor John Robert Burke
Department of Physics and Astronomy
San Francisco State University
San Francisco, CA 94132

1 Dr. Larry L. Howell
Department of Mechanical Engineering
Brigham Young University
Provo, UT 84602

1 MS 0378
Allen C. Robinson, 1431

1 MS 1310
Steven N. Kempka, 1513

1 MS 0847
Fernando Bitsie, 1524

1 MS 0847
James M. Redmond, 1524

1 MS 1310
Hartono Sumali, 1524

1 MS 0557
Thomas J. Baca, 1525

1 MS 0557
David S. Epp, 1525

1 MS 0382
Kevin D. Copps, 1543

1 MS 1152
Joseph D. Kotulski, 1652

1 MS 1080
David R. Sandison, 1769

1 MS 1310
Michael S. Baker, 1769-1

1 MS 1310
Mark R. Platzbecker, 1769-1

1 MS 1310
Danelle M. Tanner, 1769-1

2 MS 1310
Jonathan W. Wittwer, 1769-1

1 MS 0447
Judd A. Rohwer, 2111

1 MS 0482
Eddie R. Hoover, 2123

1 MS 0482
Joel B. Wirth, 2123

1 MS 0319
John R. Fellerhoff, 2610

1 MS 0328
James A. Wilder, 2612

1 MS 0319
Mary E. Gonzales, 2613

1 MS 1310
Jay Kristoffer Brotz, 2614

1 MS 1310
Coby L. Davis, 2614

5 MS 1310
Merlin K. Decker, 2614

1 MS 1310
Ernest J. Garcia, 2614

1 MS 1310
Nolan S. Finch, 2614

1 MS 1310
Rick A. Kellogg, 2614

1 MS 1310
Stephen E. Lott, 2614

5 MS 1310
John A. Mitchell, 2614

1 MS 0319
Marc A. Polosky, 2614

1 MS 0325
Darren A. Hoke, 2615

1 MS 0311
Louis S.Weichman, 2616

1 MS 0311
John W. Franklin, 2618

1 MS 0311
Charles W. Vanecek, 2618

1 MS 0311
Ron Wild, 2618

1 MS 0855
Allen R. Roach, 2732

1 MS 0437
Gerard E. Sleefe, 2810

1 MS 0437
Michael J. McGlaun, 2830

1 MS 1310
Jack W. Smith, 2996

1 MS 9154
Edward B. Talbot, 8222

1 MS 9042
Nathan Spencer, 8774

1 MS 0405
Ronald D. Pedersen, 12346

3 MS 9018
Central Technical Files, 8945-1

2 MS 0899
Technical Library, 9616

1 MS 0612
Review & Approval Desk, 9612

1 MS 0161
Patent and Licensing Office,
11500

1 MS 0123
D. Chavez, LDRD Office, 1011